Journal of Sound and Vibration 333 (2014) 3505–3521

Contents lists available at ScienceDirect

Journal of Sound and Vibration

journal homepage: www.elsevier.com/locate/jsvi

A hierarchy of high-order theories for symmetric modes in an elastic layer

S.V. Sorokin [a,*], C.J. Chapman [b]

[a] Department of Mechanical and Manufacturing Engineering, Aalborg University Fibigerstraede 16, DK 9220 Aalborg, Denmark
[b] Department of Mathematics, University of Keele Keele, Staffordshire, ST5 5BG, United Kingdom

ARTICLE INFO

Article history:
Received 14 November 2013
Received in revised form
28 February 2014
Accepted 4 March 2014
Handling Editor: S. Ilanko
Available online 16 April 2014

ABSTRACT

A hierarchy of high-order theories for symmetric modes in an infinitely long elastic layer of the constant thickness is derived by means of the inertia-corrected polynomial approximations. For each member of the hierarchy, boundary conditions for layers of the finite length are formulated. The forcing problems at several approximation levels are solved with the use of the bi-orthogonality conditions. Accuracy of these approximations is assessed by comparison of results with the exact solution of the Rayleigh–Lamb problem. Special attention is paid to the power flow analysis in alternative modal excitation cases and to the applicability of the Saint-Venant's principle in stationary elasto-dynamics.

1. Introduction

For virtually all technical applications, there is a strong demand to model the generation and transmission of the vibro-acoustic energy in structures exposed to a time-harmonic excitation, which is typically categorised into the low-, high- or mid-frequency range. The preferred tools for modelling wave propagation vary from the deterministic ones at low frequencies to the statistical ones at high frequencies. The deterministic low frequency tools are based on finite element, or spectral element, or similar methods, which, in their turn, utilise equations of 3D elasto-dynamics, or 2D equations of thin plates/shells theories, or one-dimensional equations of classical beams/rods theories. The obvious choice for slender structures is the latter ones, which, however, imposes severe limitations on the range of applicability. Therefore, it is of significant practical value to develop advanced analytical one-dimensional models, or theories, valid for both low-, and mid-frequency ranges. Accuracy of such models should be verified not by comparison with inherently approximate solutions, as those obtained, e.g., with 3D finite elements, but rather with exact analytical solutions of equations of elasto-dynamics.

The purpose of this paper is to derive a hierarchy of models of this type, and to apply those for analysis of free and forced wave motions in a straight elastic layer with constant thickness and traction-free surfaces, i.e., for solving the classical Rayleigh–Lamb problem. The solution of this problem is presented in standard texts [1–3]. These references also address an assessment of the validity ranges of the elementary, or engineering, theories (Bernoulli–Euler and Timoshenko for the skew-symmetric modes, Bernoulli and Mindlin–Herrmann for the symmetric modes) for predictions of free wavenumbers and possibilities to develop high-order models.

The quest for such theories has a long history. The common method to derive reduced models from elasto-dynamics is to employ the smallness of the thickness of a layer. This research track may involve formulation of 'the dynamic theory of thin

* Corresponding author.
E-mail addresses: svs@m-tech.aau.dk (S.V. Sorokin), c.j.chapman@maths.keele.ac.uk (C.J. Chapman).

http://dx.doi.org/10.1016/j.jsv.2014.03.005
0022-460X/

walled linearly elastic bodies, treated as an asymptotic branch of 3D elasticity free of ad hoc assumptions ([4], p.1). The book [4] and subsequent publications of its authors give an impressive account of productivity of this methodology. Another approach to derive reduced models from elasto-dynamics is to use Taylor series in the transverse coordinate to expand displacements. It has been applied in many publications, with [1,2,5,6] being just a few examples. The main point in the asymptotic models is the consistency of formulation of traction-free boundary conditions at the surfaces of a layer with the exact one. However, the mathematical background of these theories is much more advanced, than of the elementary engineering theories, and this may be regarded as a disadvantage.

An alternative approach, in a way, extends the kinematic hypotheses used in the classical engineering theories. The displacements are expanded in appropriate sets of orthogonal polynomials in transverse coordinate, and these series are truncated [7,8]. Then differential equations of motion are derived from equations of elastodynamics by means of the Galerkin method [7] or the variational principle [8]. Due to the symmetry of a layer with respect to its mid-plane, this procedure yields two uncoupled systems of differential equations describing symmetric (with respect to mid-plane) and skew-symmetric modes. The first terms in series for displacements are polynomials of the zeroth and the first order in the transverse coordinate. Therefore, the low-order approximations become identical to the conventional elementary theories, which employ the 'plane cross-section' hypothesis. As higher-order polynomials are added, this approach resembles a modal decomposition across the thickness of a layer.

However, it suffers two major drawbacks. First, a polynomial decomposition for displacements, once chosen, is kept the same at any frequency, whereas the shapes of exact modes obtained by solving the Rayleigh–Lamb problem are frequency-dependent. As well-known, the across thickness shape of the first skew-symmetric mode gradually transforms from the shape very accurately described by the 'plane cross section' kinematic assumption (at low frequencies) to the shape of the Rayleigh surface wave at high frequencies. Inability to capture such a transformation hampers accuracy of the model. Second, this decomposition is not suitable to satisfy the traction-free boundary conditions at the lateral surfaces of a layer. In effect, an elastic layer with no tractions at the surfaces is replaced by a layer with frequency-dependent tractions.

Given these reservations, the expectations to obtain very accurate results by means of the polynomial approximation cannot be too high. However, an asymptotic consistency of the 'zeroth order' Bernoulli–Euler (for skew-symmetric modes) and Bernoulli (for symmetric modes) models with the low-frequency–small wavenumber limits of the exact solutions and, in particular, the generally recognised usefulness of the Timoshenko model at frequencies up to and slightly above the cut-on frequency of the second skew-symmetric mode suggest that this methodology, perhaps, after some refinement, may be used to model wave propagation in the mid-frequency range.

This analytical modelling, if successful, should provide a meaningful alternative to existing numerical techniques based on a discretisation of continuous elastic waveguides. The preferred method to derive such high-order theories is via variation of the action integral, because in the course of derivation the boundary conditions at the ends of a layer are formulated. It is particularly useful for analysis of the forced response of an elastic layer as well as for analysis of the mode conversion effects at an inhomogeneity such as, e.g., a joint between layers with different properties.

The skew-symmetric (flexural) modes in an elastic layer have gained much more attention in the literature, than symmetric ones. The high-order theories for flexural waves have been discussed in [1–3,5–8,9] and many other papers. The similar work on symmetric modes is reported in fewer publications. The expansion of displacements in a series on Legendre polynomials has been employed in [1,7,8,10–12]. The truncation level in the series determines the level of the multi-modality of a theory. The alternative one- and two-mode theories are compared in [10,11]. In [11], the three-mode theory is also discussed with the reference to [8]. However, the derivation of the governing equations attributed to this theory is not given, and the non-symmetry of those is not commented in [11]. The pioneering work on the three-mode theory was done by Mindlin and Medick in [12]. They introduced and employed an idea of matching of approximate dispersion curves to their exact counterparts, which is also employed in the present paper.

The paper is structured as follows. The exact solution and three classical one-mode models are described in Sections 2 and 3 respectively to set up the stage for further advances. Sections 4 and 5 are concerned with derivation and fine matching of the three- and five-mode polynomial approximations respectively. The bi-orthogonality conditions are derived, and the analysis of forced response of an infinitely long elastic layer exposed to symmetric excitation is presented in Section 6.

2. Exact solution of the Rayleigh–Lamb problem for symmetric modes

The dispersion equation for symmetric modes can be found in any text on elastodynamics, and it is reproduced here for consistency. We consider stationary time-harmonic, $\exp(-\mathrm{i}\omega t)$, free waves at the frequency ω in an infinitely long straight elastic layer of constant thickness h with traction-free boundary conditions in plane strain state. The elastic properties are specified by velocities of dilatation and shear waves, c_1 and c_2; the inertia of a layer is specified by the mass density ρ. The standard Lamé decomposition of the displacement field $\mathbf{u} \equiv (u, v, 0)^T$ is employed: $\mathbf{u} = \nabla \cdot \Phi + \nabla \times \mathbf{i}_Z \Psi$. The potentials Φ and Ψ are governed by the Helmholtz equations as follows:

$$\nabla^2 \Phi + \frac{\omega^2}{c_1^2} \Phi = 0; \quad \nabla^2 \Psi + \frac{\omega^2}{c_2^2} \Psi = 0. \tag{1}$$

Due to the symmetry in the boundary conditions at $y_{\mathrm{dim}} = \pm h/2$, the symmetric and skew-symmetric modes are considered independent from each other. For free time-harmonic symmetric modes, the conventional spatial dependence is

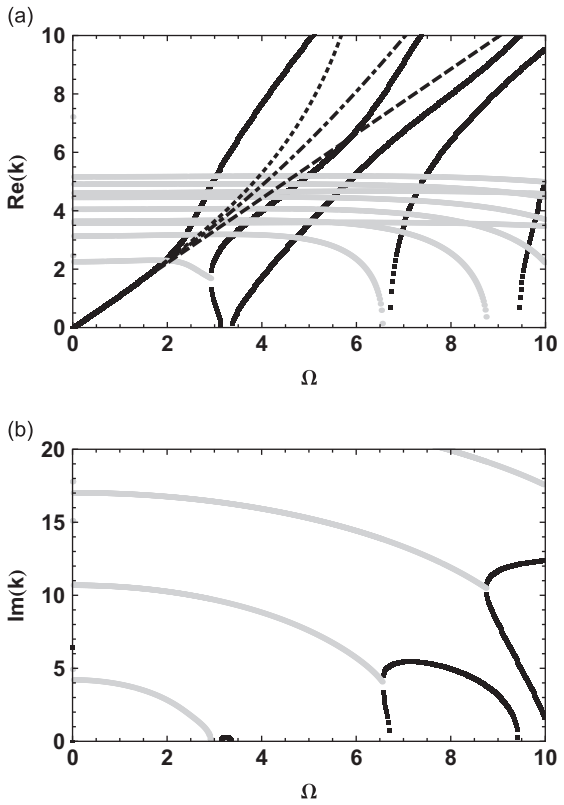

Fig. 1. The Rayleigh–Lamb dispersion diagrams: (a) real parts and (b) imaginary parts of wavenumbers. Black curves: purely real and purely imaginary wavenumbers, grey curves: complex-valued wavenumbers. Dashed line: the Bernoulli model, dashed–dotted line: the Rayleigh–Love model; dotted line: the Bishop model.

taken as $\exp(ik_{\mathrm{dim}}x_{\mathrm{dim}})$, so that the dispersion equation is ([2], p. 223)

$$\frac{\tan(q/2)}{\tan(p/2)} = -\frac{4k^2pq}{(q^2-k^2)^2} \tag{2}$$

In this equation, $p^2=(\omega h/c_1)^2-(k_{\mathrm{dim}}h)^2$, $q^2=(\omega h/c_2)^2-(k_{\mathrm{dim}}h)^2$. It is convenient to transform the equation to non-dimensional parameters with displacements and wavenumbers scaled to the thickness of an elastic layer h. The frequency parameter is introduced as $\Omega=\omega h/c_1$. Then $p^2=\Omega^2-k^2$ and $q^2=\alpha^2\Omega^2-k^2$. The notation $\alpha=c_1/c_2\equiv\sqrt{2(1-\nu)/(1-2\nu)}$, where ν is the Poisson ratio, is used hereafter. The dispersion diagram is shown in Fig. 1 for $\nu=0.3$ as the reference for approximate theories considered in Sections 3–5. Grey curves present real and imaginary parts of complex-valued wavenumbers. Black curves in Fig. 1a present purely real wavenumbers. In Fig. 1b, curves of the same colour are plotted after purely imaginary ones.

As well-known, in the low frequency–small wavenumber limit, the dispersion Eq. (2) is reduced to the elementary form:

$$k^2=\frac{\alpha^4}{4(\alpha^2-1)}\Omega^2 \tag{3}$$

This asymptotically correct dispersion equation serves as the checklist of trustworthiness of all reduced theories discussed in Sections 3–5.

3. The classical one-mode theories

We begin with a fairly trivial case, which, however, sets up the stage for all subsequent advances. The classical one-mode theories clarify the link of the methodology we pursuit in this paper with the 'plane cross-section' assumption and highlight the inherent defiance of the approximate theories.

The plane strain problem formulation introduced in Section 2 is used. The displacement field in an elastic layer is approximated with the 'plane cross-section' hypothesis:

$$u(x,y,t)=U_0(x,t)1 \tag{4}$$

At this stage, no *a priori* approximation is imposed on the transverse displacement $v(x,y,t)$.

The strains are

$$\varepsilon_x(x,y,t)=\frac{\partial U_0(x,t)}{\partial x},\quad \varepsilon_y(x,y,t)=\frac{\partial v(x,y,t)}{\partial y},\quad \varepsilon_{xy}(x,y,t)=\frac{\partial v(x,y,t)}{\partial x} \tag{5}$$

The non-dimensional stresses (scaled with ρc_2^2) are

$$\sigma_x(x,y,t)=\alpha^2\left[\varepsilon_x(x,y,t)+\varepsilon_y(x,y,t)\right]-2\varepsilon_y(x,y,t)=\alpha^2\frac{\partial U_0(x,t)}{\partial x}+(\alpha^2-2)\frac{\partial v(x,y,t)}{\partial y}, \tag{6a}$$

$$\sigma_y(x,y,t)=\alpha^2\left[\varepsilon_x(x,y,t)+\varepsilon_y(x,y,t)\right]-2\varepsilon_x(x,y,t)=(\alpha^2-2)\frac{\partial U_0(x,t)}{\partial x}+\alpha^2\frac{\partial v(x,y,t)}{\partial y} \tag{6b}$$

$$\sigma_{xy}(x,y,t)=\varepsilon_{xy}(x,y,t)=\frac{\partial v(x,y,t)}{\partial x} \tag{6c}$$

The action integral is formulated in the standard form: $H=\int_{t_1}^{t_2}[T-V]\mathrm{d}t$.
The kinetic energy is

$$T=\frac{1}{2}\rho\int_{-1/2}^{1/2}\int_a^b\left[\left(\frac{\partial U_0(x,t)}{\partial t}\right)^2+\left(\frac{\partial v(x,y,t)}{\partial t}\right)^2\right]\mathrm{d}x\mathrm{d}y \tag{7}$$

The potential energy is

$$V=\frac{1}{2}\rho c_2^2\int_{-1/2}^{1/2}\int_a^b\left[\left|\left(\alpha^2\frac{\partial U_0(x,t)}{\partial x}+(\alpha^2-2)\frac{\partial v(x,y,t)}{\partial y}\right)\frac{\partial U_0(x,t)}{\partial x}\right.\right.$$
$$\left.\left.+\left((\alpha^2-2)\frac{\partial U_0(x,t)}{\partial x}+\alpha^2\frac{\partial v(x,y,t)}{\partial y}\right)\frac{\partial v(x,y,t)}{\partial y}+\left(\frac{\partial v(x,y,t)}{\partial x}\right)^2\right]\mathrm{d}x\mathrm{d}y \tag{8}$$

The transverse displacement is found from the condition that the transverse normal stresses vanish not only at the surfaces $y=\pm 1/2$, as specified in the exact problem formulation, but in the whole volume of an elastic layer:

$$\sigma_y(x,y,t)=0. \tag{9}$$

This condition defines the function $v(x,y,t)$ as

$$v(x,y,t)=\frac{(2-\alpha^2)}{\alpha^2}\frac{\partial U_0(x,t)}{\partial x}y. \tag{10}$$

Then integration in the y-coordinate in ((7) and (8)) gives, respectively

$$T=\frac{1}{2}\rho\int_a^b\left[\left(\frac{\partial U_0(x,t)}{\partial t}\right)^2+\frac{1}{12}\frac{(2-\alpha^2)^2}{\alpha^4}\left(\frac{\partial^2 U_0(x,t)}{\partial x\partial t}\right)^2\right]\mathrm{d}x \tag{11a}$$

$$V=\frac{1}{2}\rho c_2^2\int_a^b\left[\frac{4(\alpha^2-1)}{\alpha^2}\left(\frac{\partial U_0(x,t)}{\partial x}\right)^2+\frac{1}{12}\frac{(2-\alpha^2)^2}{\alpha^4}\left(\frac{\partial U_0^2(x,t)}{\partial x^2}\right)^2\right]\mathrm{d}x \tag{11b}$$

The governing equations for three classical theories are obtained when Hamilton's principle, $\delta H=0$, is applied to the action integral with its components defined as (11)

- So-called Bishop theory is derived without any further simplifications:

$$-\frac{\partial^2 U_0(x,t)}{\partial t^2}+\frac{1}{12}\frac{(2-\alpha^2)^2}{\alpha^4}\frac{\partial^4 U_0(x,t)}{\partial x^2\partial t^2}+\frac{4(\alpha^2-1)}{\alpha^2}c_2^2\frac{\partial^2 U_0(x,t)}{\partial x^2}-\frac{1}{12}\frac{(2-\alpha^2)^2}{\alpha^4}c_2^2\frac{\partial U_0^4(x,t)}{\partial x^4}=0 \tag{12}$$

  This is, strictly speaking, not a one-mode theory, because it predicts two pairs of waves, travelling/decaying in opposite directions. However, the physical relevance of the imaginary wavenumbers is questionable, and this model is categorised as a refinement of the subsequent two models.
- The Rayleigh–Love theory is derived under assumption that the second term in formula (11b) is negligible:

$$-\frac{\partial^2 U_0(x,t)}{\partial t^2}+\frac{1}{12}\frac{(2-\alpha^2)^2}{\alpha^4}\frac{\partial^4 U_0(x,t)}{\partial x^2\partial t^2}+\frac{4(\alpha^2-1)}{\alpha^2}c_2^2\frac{\partial^2 U_0(x,t)}{\partial x^2}=0 \tag{13}$$

  This simplification means that the potential energy of shear deformation is neglected.
- The Bernoulli theory is derived when the second terms in both formulas (11a) and (11b) are neglected:

$$-\frac{\partial^2 U_0(x,t)}{\partial t^2}+\frac{4(\alpha^2-1)}{\alpha^2}c_2^2\frac{\partial^2 U_0(x,t)}{\partial x^2}=0 \tag{14}$$

The difference from the Rayleigh–Love theory is that shear deformation is neglected both in the potential and in the kinetic energy of an elastic layer.

The boundary conditions at the edges of an elastic layer $x=a$, $x=b$ are readily obtained as the non-integral terms when variations are taken. These conditions in the Bernoulli theory are concerned with

$$U_0(x,t) \text{ or } F_0(x,t) \equiv -\frac{4(\alpha^2-1)}{\alpha^2}\frac{\partial U_0(x,t)}{\partial x}. \tag{15}$$

In the Rayleigh–Love theory, this couple is

$$U_0(x,t) \text{ or } F_0(x,t) \equiv -\frac{4(\alpha^2-1)}{\alpha^2}\frac{\partial U_0(x,t)}{\partial x}-\frac{1}{12}\frac{(2-\alpha^2)^2}{\alpha^4}\frac{1}{c_2^2}\frac{\partial^3 U_0(x,t)}{\partial x\partial t^2}. \tag{16}$$

In the case of the Bishop theory, which features the fourth derivative of the axial displacement, the boundary conditions are formulated with respect to

$$U_0(x,t) \text{ or } F_0(x,t) \equiv -\frac{4(\alpha^2-1)}{\alpha^2}\frac{\partial U_0(x,t)}{\partial x}-\frac{1}{12}\frac{(2-\alpha^2)^2}{\alpha^4}\frac{1}{c_2^2}\frac{\partial^3 U_0(x,t)}{\partial x\partial t^2}+\frac{1}{12}\frac{(2-\alpha^2)^2}{\alpha^4}\frac{\partial U_0^3(x,t)}{\partial x^3} \tag{17a}$$

$$\frac{\partial U_0(x,t)}{\partial x} \text{ or } -\frac{1}{12}\frac{(2-\alpha^2)^2}{\alpha^4}\frac{\partial U_0^2(x,t)}{\partial x^2} \tag{17b}$$

The physical interpretation of the boundary conditions in the Bernoulli theory is obvious: the force resultant of normal stresses in the axial direction is proportional to $\varepsilon_x(x,y,t)=\partial U_0(x,t)/\partial x$. In the Rayleigh–Love theory, this force acquires the dynamic component. The physical interpretation of the boundary conditions in the Bishop theory is less obvious, but this issue lies beyond the scope of this paper.

It is a trivial matter to show that all three theories are asymptotically consistent with the exact solution of the Rayleigh–Lamb problem in the low frequency–small wavenumber limit. Indeed, the standard substitution $U_0(x,t)=U_{00}\exp(\mathrm{i}kx-\mathrm{i}\omega t)$ to the differential Eq. (12) yields the dispersion equation in the familiar form:

$$\alpha^2\Omega^2-\frac{4(\alpha^2-1)}{\alpha^2}k^2+\frac{1}{12}\frac{(2-\alpha^2)^2}{\alpha^2}\Omega^2k^2-\frac{1}{12}\frac{(2-\alpha^2)^2}{\alpha^4}k^4=0 \tag{18}$$

The first two terms are present in the dispersion equations of all three theories, the third one is added when the Rayleigh–Love theory is considered, and the last one is accounted for in the Bishop theory. The leading order terms in the vicinity of the origin of coordinates in dispersion diagram give Eq. (3). The straight dashed line in Fig. 1a is plotted for the Bernoulli model. Dashed–dotted curve and dotted curve are plotted after the Rayleigh–Love and Bishop theories. As seen, the corrections introduced by these theories are asymptotically insignificant in the low frequency–small wavenumber limit, and their predictions are rather poor elsewhere.

The Bernoulli theory is derived under assumption that shear stresses are absent in the whole layer including surfaces, $\sigma_{xy}(x,y,t)=0$. Taking into account the condition (9) common for all three theories, we notice that this elementary theory is consistent with the traction-free boundary conditions at $y=\pm 1/2$. In contrast, the two 'refined' theories are not. However, the Bernoulli theory is also inconsistent in the sense, that the assumption $\sigma_{xy}(x,y,t)=0$ contradicts the result (10) for the transverse displacement.

The quest for high-order reduced theories of elastic wave propagation is challenged by the demand of the asymptotic consistency of such theories with the exact Rayleigh–Lamb theory. As discussed in Section 1, a substantial effort has been made to meet this challenge in the mathematically rigorous way. In what follows, an alternative strategy is adopted. The defiance in the boundary conditions at the surfaces of a layer is not attempted to be recovered. The main effort is to reproduce the exact dispersion diagram by means of a reduced theory as accurately as possible. Another goal is to formulate the loading and boundary conditions at the edges of a layer consistently. To accomplish both tasks, Hamilton's principle is chosen as a tool for derivation.

4. The three-mode theory

In literature, much attention has been paid to the formulation of a theory, analogues to the Timoshenko theory of flexural waves, i.e. describing the first and the second branches of dispersion diagram for symmetric modes as shown in Fig. 1. Such a theory is known as the Herrmann–Mindlin theory [1,10,11]. It is less successful than the Timoshenko theory in approximation of exact dispersion curves, see [1], p. 156.

The reason for that may be related to the details of the extending approximation (4) for displacements. To capture the second branch in the Herrmann–Mindlin theory, the transverse displacement is assumed to be, in contrast with the one-mode theory, an independent linear function of the transverse coordinate:

$$v(x,y,t)=\Psi_1(x,t)\cdot y \tag{19}$$

No terms are then added to the expansion of the axial displacement (4). The difference between the Herrmann–Mindlin theory and the one-mode theory is that the transverse displacement $v(x,y,t)$ is unrelated to $u(x,y,t)$ via the traction-free boundary conditions at $y=\pm 1/2$. Thus, the variational procedure in the Herrmann–Mindlin theory involves two independent functions (4) and (19). The system of two differential equations of the second order each is obtained, and the dispersion equation becomes a fourth-order polynomial both in frequency and wavenumber, see [10,11] for details.

However, a view on the hierarchy of approximations may be different. It is certainly reasonable to consider formula (4) as the zeroth-order approximation, but, at the next approximation level, both displacements can be expanded with additional terms, see also [7,8,11,12]:

$$u(x,y,t)=U_0(x,t)\cdot 1+\Phi_2(x,t)\cdot(1-12y^2),\quad v(x,y,t)=\Psi_1(x,t)\cdot y \tag{20}$$

The functions in the y-coordinate introduced in Eqs. (20) are Legendre polynomials adjusted for the interval $(-1/2, 1/2)$. As discussed in Section 1, this approximation does not remove the defiance in the traction-free boundary conditions at $y=\pm 1/2$.

Substitution of the functions (20) to the kinetic and potential energies and integration over thickness give the following expressions:

$$T=\frac{1}{2}\rho\int_a^b\left[\left(\frac{\partial U_0(x,t)}{\partial t}\right)^2+\frac{1}{12}\left(\frac{\partial \Psi_1(x,t)}{\partial t}\right)^2+\frac{4}{5}\left(\frac{\partial \Phi_2(x,t)}{\partial t}\right)^2\right]\mathrm{d}x, \tag{21a}$$

$$V=\frac{1}{2}\rho c_2^2\int_a^b\left[\alpha^2\left(\frac{\partial U_0(x,t)}{\partial x}\right)^2+\frac{1}{12}\left(\frac{\partial \Psi_1(x,t)}{\partial x}\right)^2+\frac{4}{5}\alpha^2\left(\frac{\partial \Phi_2(x,t)}{\partial x}\right)^2+(2\alpha^2-4)\frac{\partial U_0(x,t)}{\partial x}\Psi_1(x,t).\right.$$
$$\left.-4\frac{\partial \Psi_1(x,t)}{\partial x}\Phi_2(x,t)+\alpha^2(\Psi_1(x,t))^2+48(\Phi_2(x,t))^2\right]\mathrm{d}x, \tag{21b}$$

Further substitution to the action integral and taking variations give the following system of differential equations:

$$\alpha^2\frac{\partial^2 U_0(x,t)}{\partial x^2}-\frac{1}{c_2^2}\frac{\partial^2 U_0(x,t)}{\partial t^2}-(2-\alpha^2)\frac{\partial \Psi_1(x,t)}{\partial x}=0, \tag{22a}$$

$$(2-\alpha^2)\frac{\partial U_0(x,t)}{\partial x}+\frac{1}{12}\frac{\partial^2 \Psi_1(x,t)}{\partial x^2}-\alpha^2\Psi_1(x,t)-\frac{1}{12}\frac{1}{c_2^2}\frac{\partial^2 \Psi_1(x,t)}{\partial t^2}-2\frac{\partial \Phi_2(x,t)}{\partial x}=0, \tag{22b}$$

$$2\frac{\partial \Psi_1(x,t)}{\partial x}+\frac{4}{5}\alpha^2\frac{\partial^2 \Phi_2(x,t)}{\partial x^2}-48\Phi_2(x,t)-\frac{4}{5}\frac{1}{c_2^2}\frac{\partial^2 \Phi_2(x,t)}{\partial t^2}=0. \tag{22c}$$

These equations are the Euler–Lagrange equations for the action integral and, therefore, have the symmetry properties. The boundary conditions at the edges $x=a$, $x=b$ are concerned with the following pairs of generalised forces and displacements:

$$F_0(x,t)\equiv\alpha^2\frac{\partial U_0(x,t)}{\partial x}+(\alpha^2-2)\Psi_1(x,t)\ \text{ and }\ U_0(x,t) \tag{23a}$$

$$F_1(x,t)\equiv\frac{1}{12}\frac{\partial \Psi_1(x,t)}{\partial x}-2\Phi_2(x,t)\ \text{ and }\ \Psi_1(x,t) \tag{23b}$$

$$F_2(x,t)\equiv\frac{4}{5}\alpha^2\frac{\partial \Phi_2(x,t)}{\partial x}\ \text{ and }\ \Phi_2(x,t) \tag{23c}$$

It is useful to notice that the formulas (23) may also be obtained by direct integration of the stress components in the following way:

$$F_0(x,t)=\int_{-1/2}^{1/2}\sigma_x(x,y,t)\cdot 1\mathrm{d}y,\quad F_1(x,t)=\int_{-1/2}^{1/2}\sigma_{xy}(x,y,t)\cdot y\mathrm{d}y,\quad F_2(x,t)=\int_{-1/2}^{1/2}\sigma_x(x,y,t)\cdot(1-12y^2)\mathrm{d}y \tag{24}$$

These formulas provide a physical interpretation of the generalised forces as weighted resultants of normal and shear stresses in the cross-section of a layer. The related weight functions are exactly the polynomials chosen to approximate the displacement field in the y-coordinate.

The dispersion equation is readily available after substituting with Eqs. (22):

$$U_0(x,t)=U_{00}\exp(\mathrm{i}kx-\mathrm{i}\omega t),\quad \Psi_1(x,t)=\Psi_{10}\exp(\mathrm{i}kx-\mathrm{i}\omega t),\quad \Phi_2(x,t)=\Phi_{20}\exp(\mathrm{i}kx-\mathrm{i}\omega t).$$

The system of linear homogeneous algebraic equations with respect to U_{00}, Ψ_{10}, and Φ_{20} has the form:

$$(-\alpha^2k^2+\alpha^2\Omega^2)U_{00}-(2-\alpha^2)\mathrm{i}k\Psi_{10}=0 \tag{25a}$$

$$(2-\alpha^2)\mathrm{i}kU_{00}+\left(-\frac{1}{12}k^2-\alpha^2+\frac{1}{12}\alpha^2\Omega^2\right)\Psi_{10}-2\mathrm{i}k\Phi_{20}=0 \tag{25b}$$

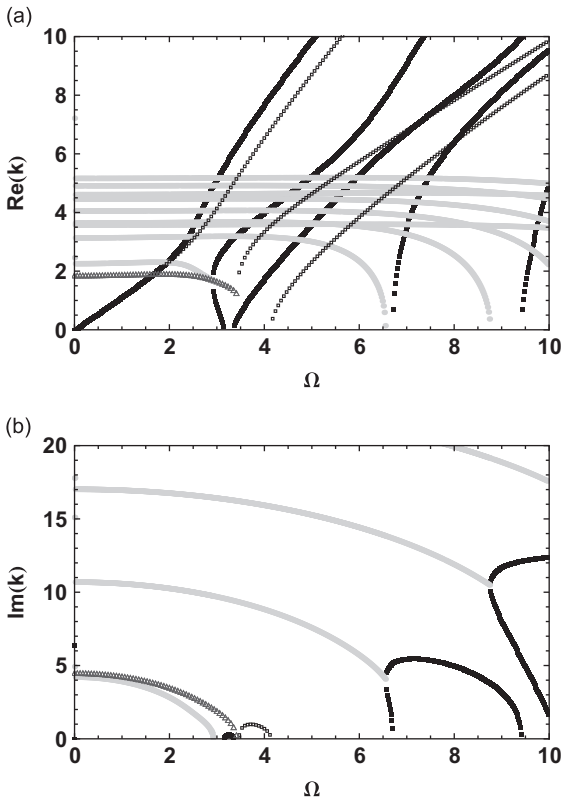

Fig. 2. Comparison of the uncorrected three-mode dispersion diagram with the Rayleigh–Lamb solution: (a) real parts and (b) imaginary parts of wavenumbers.

$$2ik\Psi_{10}+\left(-\frac{4}{5}\alpha^2k^2-48+\frac{4}{5}\alpha^2\Omega^2\right)\Phi_{20}=0 \tag{25c}$$

Due to the symmetry property of Eqs. (20), this system of algebraic equations has a real-valued determinant. Equating it to zero gives the dispersion equation of the sixth order both in the frequency parameter and the wavenumber. The dispersion diagram obtained by solving this equation is compared with the exact solution in Fig. 2. Triangle-designated curves in Fig. 2 present real and imaginary parts of complex-valued wavenumber; square-designated curves present purely real and purely imaginary wavenumbers obtained from the determinant of the system (25). As seen, there are significant discrepancies in the approximate theory, which manifest themselves already for the magnitudes of cut-on frequencies, see Fig. 2a. Nevertheless, the correct low-frequency–small wavenumber limit (3) is preserved.

To extend the agreement between the approximate and exact dispersion diagrams to the emerging branches, some correction factors should be introduced. The idea to use correction factor is typical for approximate theories of this type, with the obvious example being the Timoshenko theory. In our previous work [13], the inertia-correction factor was introduced in this framework as an alternative for the standard shear correction factor. Another example is the paper [12], in which the correction coefficients are introduced in a different way.

The inertia correction factors are put in the formula (21a) for the kinetic energy as follows:

$$T=\frac{1}{2}\rho\int_a^b\left[\left(\frac{\partial U_0(x,t)}{\partial t}\right)^2+\frac{1}{12}C_{11}\left(\frac{\partial\Psi_1(x,t)}{\partial t}\right)^2+\frac{4}{5}C_{12}\left(\frac{\partial\Phi_2(x,t)}{\partial t}\right)^2\right]\mathrm{d}x \tag{26}$$

Then the two linear algebraic Eqs. (25b) and (25c) become:

$$(2-\alpha^2)\mathrm{i}kU_{00}+\left(-\frac{1}{12}k^2-\alpha^2+\frac{1}{12}C_{11}\alpha^2\Omega^2\right)\Psi_{10}-2\mathrm{i}k\Phi_{20}=0 \tag{27a}$$

$$2ik\Psi_{10}+\left(-\frac{4}{5}\alpha^2k^2-48+\frac{4}{5}C_{12}\alpha^2\Omega^2\right)\Phi_{20}=0 \tag{27b}$$

The magnitudes of cut-on frequencies obtained from the exact dispersion Eq. (2) are

$$\Omega_{\mathrm{cut-on},1}=\pi,\quad \Omega_{\mathrm{cut-on},2}=\frac{2\pi}{\alpha}$$

Equating wavenumbers to zero in the determinant of the system of Eqs. (25a), (27a), and (27b) we obtain the following formulas for cut-on frequencies in the approximate three-mode theory:

$$\Omega_{\text{cut-on},1}=\frac{2\sqrt{3}}{\sqrt{C_{11}}},\quad \Omega_{\text{cut-on},2}=\frac{2\sqrt{15}}{\alpha\sqrt{C_{12}}}$$

Then the matching gives $C_{11}=12/\pi^2$, $C_{12}=15/\pi^2$. The system of governing differential equations acquires the form:

$$\alpha^2\frac{\partial^2 U_0(x,t)}{\partial x^2}-\frac{1}{c_2^2}\frac{\partial^2 U_0(x,t)}{\partial t^2}-(2-\alpha^2)\frac{\partial \Psi_1(x,t)}{\partial x}=0$$

$$(2-\alpha^2)\frac{\partial U_0(x,t)}{\partial x}+\frac{1}{12}\frac{\partial^2 \Psi_1(x,t)}{\partial x^2}-\alpha^2\Psi_1(x,t)-\frac{1}{\pi^2}\frac{1}{c_2^2}\frac{\partial^2 \Psi_1(x,t)}{\partial t^2}-2\frac{\partial \Phi_2(x,t)}{\partial x}=0$$

$$2\frac{\partial \Psi_1(x,t)}{\partial x}+\frac{4}{5}\alpha^2\frac{\partial^2 \Phi_2(x,t)}{\partial x^2}-48\Phi_2(x,t)-\frac{12}{\pi^2}\frac{1}{c_2^2}\frac{\partial^2 \Phi_2(x,t)}{\partial t^2}=0 \tag{28}$$

With the inertia correction factors accounted for, the dispersion diagram plotted after the three-mode theory agrees fairly well with the exact solution, see Fig. 3. The designations used to plot the dispersion curves are the same as in Fig. 2. It should be noted that the inertia correction factors do not affect the formulation of the non-integral terms in the variational procedure. Therefore, the boundary conditions (23) are not altered.

This idea has not been proposed in [7,8], where only Eqs. (25) was derived, but its counterpart can be found in [12]. However, its implementation in this reference is different. The free parameters to match dispersion curves are introduced there to match the exact and approximate dispersion diagrams at zero wavenumber that is similar to our method. The difference is that amount of these coefficients exceeds the amount of branches of dispersion curves, and it brings an ambiguity to the matching procedure. In contract, the two inertia-correction factors in (26) are uniquely defined by exact cut-on frequencies. Furthermore, we may claim that the inertia correction factor in the first term in (26) equals unity, because both the zero value of the first cut-on frequency and the slope at the origin of coordinates are predicted correctly. Therefore, the introduction of inertia correction factors to match cut-on frequencies is a substantial development of the polynomial approximation method.

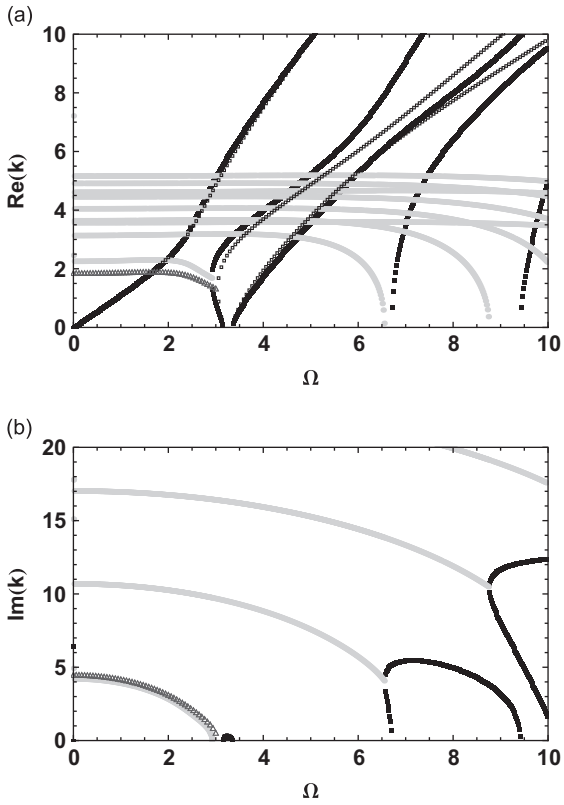

Fig. 3. Comparison of the inertia-corrected three-mode dispersion diagram with the Rayleigh–Lamb solution: (a) real parts and (b) imaginary parts of wavenumbers.

5. The five-mode theory

The next member in the hierarchy of the multimode approximate theories is the one, which should satisfactory describe the shape of the first five branches in the diagram as shown in Fig. 1a. To derive such a theory, two terms (with the y-dependence of scaled Legendre polynomials) are added in expansion (20):

$$u(x,y,t)=U_0(x,t)1+\Phi_2(x,t)(1-12y^2)+\Phi_4(x,t)\left(\frac{9}{8}-45y^2+120y^4\right), \tag{29a}$$

$$v(x,y,t)=\Psi_1(x,t)y+\Psi_3(x,t)(3y\sqrt{7}-20y^3\sqrt{7}). \tag{29b}$$

Substitution of these functions to the action integral and taking variations by means of the symbolic manipulator Mathematica [14] give the following system of differential equations:

$$\alpha^2\frac{\partial^2 U_0(x,t)}{\partial x^2}-\alpha^2\frac{\partial^2 U_0(x,t)}{\partial t^2}-(2-\alpha^2)\frac{\partial \Psi_1(x,t)}{\partial x}+2\sqrt{7}(2-\alpha^2)\frac{\partial \Psi_3(x,t)}{\partial x}=0 \tag{30a}$$

$$(2-\alpha^2)\frac{\partial U_0(x,t)}{\partial x}+\frac{1}{12}\frac{\partial^2 \Psi_1(x,t)}{\partial x^2}-\alpha^2\Psi_1(x,t)-\frac{1}{12}\frac{1}{c_2^2}C_{21}\frac{\partial^2 \Psi_1(x,t)}{\partial t^2}-2\frac{\partial \Phi_2(x,t)}{\partial x}+2\alpha^2\sqrt{7}\Psi_3(x,t)+3\frac{\partial \Phi_4(x,t)}{\partial x}=0, \tag{30b}$$

$$2\frac{\partial \Psi_1(x,t)}{\partial x}+\frac{4}{5}\alpha^2\frac{\partial^2 \Phi_2(x,t)}{\partial x^2}-48\Phi_2(x,t)-\frac{4}{5}\frac{1}{c_2^2}C_{22}\frac{\partial^2 \Phi_2(x,t)}{\partial t^2}-4\sqrt{7}(2-\alpha^2)\frac{\partial \Psi_3(x,t)}{\partial x}+72\Phi_4(x,t)=0, \tag{30c}$$

$$-2\sqrt{7}(2-\alpha^2)\frac{\partial U_0(x,t)}{\partial x}+2\alpha^2\sqrt{7}\Psi_1(x,t)+4\sqrt{7}(2-\alpha^2)\frac{\partial \Phi_2(x,t)}{\partial x}+\frac{\partial^2 \Psi_3(x,t)}{\partial x^2}-168\alpha^2\Psi_3(x,t)$$
$$-\frac{1}{c_2^2}C_{23}\frac{\partial^2 \Psi_3(x,t)}{\partial t^2}-6\sqrt{7}\frac{\partial \Phi_4(x,t)}{\partial x}=0 \tag{30d}$$

$$-3\frac{\partial \Psi_1(x,t)}{\partial x}+72\Phi_2(x,t)+6\sqrt{7}\frac{\partial \Psi_3(x,t)}{\partial x}+\alpha^2\frac{\partial^2 \Phi_4(x,t)}{\partial x^2}-360\Phi_4(x,t)-\frac{1}{c_2^2}C_{24}\frac{\partial^2 \Phi_4(x,t)}{\partial t^2}=0 \tag{30e}$$

In these equations, the inertia-correction factors C_{2n}, $n=1,2,3,4$ are introduced. To recover equations of the 'genuine' polynomial approximation, these factors should be set to unity. The Euler–Lagrange equations (30) has the same symmetry properties as Eqs. (22).

The boundary conditions at the edges $x=a$, $x=b$ are obtained as the non-integral terms in the course of by-parts integration. These are concerned with the following pairs of generalised forces and displacements:

$$F_0(x,t)\equiv\alpha^2\frac{\partial U_0(x,t)}{\partial x}+(\alpha^2-2)\Psi_1(x,t)-2\sqrt{7}(\alpha^2-2)\Psi_3(x,t)\ \text{ and }\ U_0(x,t) \tag{31a}$$

$$F_1(x,t)\equiv\frac{1}{12}\frac{\partial \Psi_1(x,t)}{\partial x}-2\Phi_2(x,t)+3\Phi_4(x,t)\ \text{ and }\ \Psi_1(x,t) \tag{31b}$$

$$F_2(x,t)\equiv\frac{4}{5}\alpha^2\frac{\partial \Phi_2(x,t)}{\partial x}+4\sqrt{7}(\alpha^2-2)\Psi_3(x,t)\ \text{ and }\ \Phi_2(x,t) \tag{31c}$$

$$F_3(x,t)\equiv\frac{\partial \Psi_3(x,t)}{\partial x}-6\sqrt{7}\Phi_4(x,t)\ \text{ and }\ \Psi_3(x,t) \tag{31d}$$

$$F_4(x,t)\equiv\alpha^2\frac{\partial \Phi_4(x,t)}{\partial x}\ \text{ and }\ \Phi_4(x,t) \tag{31e}$$

The formulas (31a–c) may be obtained from (24). The formulas (31d and e) are re-written as

$$F_3(x,t)=\int_{-1/2}^{1/2}\sigma_{xy}(x,y,t)(3y\sqrt{7}-20y^3\sqrt{7})\mathrm{d}y,\quad F_4(x,t)=\int_{-1/2}^{1/2}\sigma_x(x,y,t)\left(\frac{9}{8}-45y^2+120y^4\right)\mathrm{d}y \tag{32}$$

The dispersion equation is readily available after substitution $U_0(x,t)=U_{00}\exp(\mathrm{i}kx-\mathrm{i}\omega t)$, $\Psi_1(x,t)=\Psi_{10}\exp(\mathrm{i}kx-\mathrm{i}\omega t)$, $\Phi_2(x,t)=\Phi_{20}\exp(\mathrm{i}kx-\mathrm{i}\omega t)$, $\Psi_3(x,t)=\Psi_{30}\exp(\mathrm{i}kx-\mathrm{i}\omega t)$, $\Phi_4(x,t)=\Phi_{40}\exp(\mathrm{i}kx-\mathrm{i}\omega t)$ in (30) and equating the determinant of the system of linear algebraic equations to zero.

The inertia correction factors are determined from the conditions of matching the cut-on frequencies predicted by this theory with their exact magnitudes. These factors become:

$$C_{21}=\frac{2(25+\sqrt{355})}{9\pi^2},\quad C_{22}=\frac{3(35+\sqrt{105})}{16\pi^2},\quad C_{23}=\frac{56(25-\sqrt{355})}{9\pi^2},\quad C_{24}=\frac{9(35-\sqrt{105})}{4\pi^2} \tag{33}$$

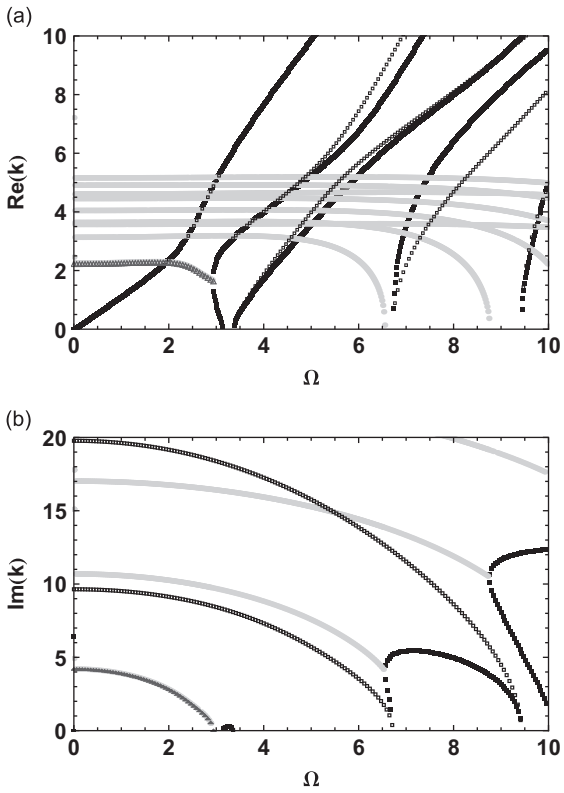

Fig. 4. Comparison of the inertia-corrected five-mode dispersion diagram with the Rayleigh–Lamb solution: (a) real parts and (b) imaginary parts of wavenumbers.

In Fig. 4, the exact dispersion diagrams are compared with the diagrams obtained with correction factors (33). All curves are designated in the same way as previously. The perfect match of the cut-on frequencies entails a good agreement between predictions of the refined five-mode model and the exact solution in a broad frequency range. The largest discrepancies occur for the fourth branch, but even in this 'worst case', wavenumbers up to $k=1.5$ are very close to each other. The dispersion diagram obtained from the direct formulation (i.e., with the correction factors set to unity) departs much more from the exact solution with the fourth and fifth cut-on frequencies lying outside the range as shown in Fig. 4. However, the asymptotically correct low frequency–small wavenumber limit (4) is preserved at any values of these factors. On balance, we conclude that the inertia-correction method very substantially improves accuracy of the five-mode theory as compared with its direct formulation.

The hierarchy of inertia-corrected multimode theories can be extended to an arbitrarily high order. The point of particular interest here is the choice of 'grid points', where the approximate dispersion curves should intersect their exact counterparts. These grid points for symmetric waves in an elastic layer are readily determined following the procedure formulated in [9] for skew-symmetric waves. However, we do not pursue this research line any further in this paper. Instead, we consider the applicability of the derived three- and five-mode theories for solving the forcing problems, and this issue is addressed in the subsequent section.

To conclude this section, we revisit the one-mode theories from the viewpoint of inertia-corrected polynomial approximations. Truncation of expansions (20) and (29) backwards to the single-term approximation (4) with the inertia-correction retained yields the following differential equation:

$$\frac{\partial^2 U_0(x,t)}{\partial x^2} - C_0 \frac{\partial^2 U_0(x,t)}{\partial t^2} = 0 \tag{34}$$

The dispersion equation is very simple: $k^2 = C_0\Omega^2$. Then the free parameter of inertia correction can be used to match this dispersion equation to the asymptotically consistent Eq. (4). This condition gives $C_0 = \alpha^4/4(\alpha^2-1)$. Thus, we conclude that the inertia-corrected one-mode theory is plausible.

6. The bi-orthogonality conditions and the forcing problem

As well-known, solving the forcing problem for a multimodal waveguide is much facilitated by a use of the bi-orthogonality condition [15–17]. We formulate this condition first in the framework of the five-mode theory. For two

distinct wavenumbers, i.e., when $k_A^2 \neq k_B^2$, it is

$$F_0^A(x)U_0^B(x)+F_2^A(x)\Phi_2^B(x)+F_4^A(x)\Phi_4^B(x)=\Psi_1^A(x)F_1^B(x)+\Psi_3^A(x)F_3^B(x) \tag{35}$$

Here the generalised forces and displacements are defined by Eqs. (31). The proof of the identity (35) is rather cumbersome, but it is straightforward and completely analogous to the proofs for other multimodal waveguides presented in [17]. Following this reference, two groups of the generalised forces and displacements are identified:

- Group 1: $F_0^A(x)$, $F_2^A(x)$, $F_4^A(x)$ with $U_0^B(x)$, $\Phi_2^B(x)$, $\Phi_4^B(x)$
- Group 2: $\Psi_1^A(x)$, $\Psi_3^A(x)$ with $F_1^B(x)$, $F_3^B(x)$ (36)

The composition of these groups is readily explained by the symmetry properties of the forces and displacements with respect to the argument $x-x_0$ (assuming the loading point located at x_0) in the 'fundamental loading cases' for an infinite layer. Specifically, if the components of one group are odd functions of this argument, then the components of the other group are even, and vice versa. At the loading point, all components of generalised forces and displacements must be continuous, except for the one, which experiences a unit jump. This discontinuous component is, by necessity, an odd function. The other members of the group, which the discontinuous component belongs to, are also odd. Therefore, to ensure continuity, each of those components must be equal to zero at the loading point. This simple rule explains the grouping of displacements and forces in the bi-orthogonality conditions.

As discussed, if the generalised unit force $F_0(x)$ is applied at $x=x_0$, then the full set of loading conditions is formulated for $x\to x_0$ as follows:

$$F_0(x-x_0)=\frac{1}{2}\mathrm{sgn}(x-x_0);\quad \Psi_1(x-x_0)=0;\quad F_2(x-x_0)=0;\quad \Psi_3(x-x_0)=0;\quad F_5(x-x_0)=0. \tag{37}$$

These loading conditions provide a system of linear algebraic equations with respect to the amplitudes of five modes with the wavenumbers satisfying radiation and decay conditions. With the bi-orthogonality being applied, the modal amplitudes are found from Eqs. (37) independently upon each other. To obtain the bi-orthogonality and the loading conditions for the three-mode theory, the generalised displacements $\Psi_3(x)$, $\Phi_4(x)$ and the generalised forces $F_3(x)$, $F_4(x)$ should be omitted in Eqs. (35)–(37).

The modal decomposition has been conveniently employed to solve the forcing problem in the exact Rayleigh–Lamb formulation, see [15,16]. In what follows, we use this solution in several generic excitation cases to assess the reliability of the models derived in the previous sections of this paper.

The dispersion diagrams shown in Fig. 1 for one-mode theories are identical in the low-frequency limit. However, the formulations of generalised forces (15)–(17) are different. Therefore, it is of interest to assess the accuracy of these theories with respect to the power flow predictions in the elementary forcing case, when normal stresses at the cross-section $x=x_0$ are uniformly distributed in the y-coordinate $x\to x_0$:

$$\sigma_x(x-x_0,y)=1\cdot\frac{1}{2}\cdot\mathrm{sgn}(x-x_0). \tag{38}$$

An infinitely long uniform waveguide with the load $\delta(x-x_0)$ is considered as two semi-infinite segments with the normal stresses at $x=x_0$ evenly distributed between them. The formulation of loading conditions in Rayleigh–Lamb forcing problem involves the absence of transverse displacement at the loaded cross-section, see [15,16]:

$$v(x-x_0,y)=0. \tag{39}$$

The reference solution of this problem is obtained with 28 modes kept in the modal decomposition ($M=28$) at each excitation frequency:

$$u(x-x_0,y)=\sum_{m=1}^{M}A_mS_{Um}(y)\exp[\mathrm{i}k_m|x-x_0|]$$
$$v(x-x_0,y)=\sum_{m=1}^{M}A_mS_{Vm}(y)\exp[\mathrm{i}k_m|x-x_0|] \tag{40}$$

The shape functions $S_{Um}(y)$, $S_{Vm}(y)$ are frequency-dependent. All propagating modes ($\mathrm{Im}k_m=0,\mathrm{Re}k_m>0$) are included in (40) along with the attenuated ones ($\mathrm{Im}k_m<0$) with the smallest $|\mathrm{Im}k_m|$. As seen in Fig. 1, in some frequency ranges the phase and group velocities of propagating waves have different signs. In these cases, the modal decomposition involves waves with the positive group velocity.

The averaged over period power flow in an elastic layer is defined as follows (see [16]):

$$P(x)=\frac{1}{2}\mathrm{Re}\int_{-1/2}^{1/2}[\sigma_x(x,y)\mathrm{i}\Omega u^*(x,y)+\sigma_{xy}(x,y)\mathrm{i}\Omega v^*(x,y)]\mathrm{d}y \tag{41}$$

The asterisk designates a complex conjugate. The power flow per unit width is scaled with $\alpha\rho hc_2^3$. In the layer with no energy dissipation, the injected power is conserved, and it is convenient to use this formula at $x=x_0$ with conditions (38)

and (39) taken into account:

$$P_{0,\mathrm{exact}} = \frac{1}{4}\mathrm{Re}\int_{-1/2}^{1/2}[\mathrm{i}\Omega u^*(x_0,y)]\mathrm{d}y \tag{42}$$

The forcing problem in the framework of one-mode Bernoulli and Rayleigh–Love theories is formulated for the axial displacement sought in the form:

$$U_0(x-x_0) = U_{00}\exp(\mathrm{i}k|x-x_0|) \tag{43}$$

This formula is written in the form conventional for derivation of Green's matrices for one-dimensional waveguides. As follows from (24a), the axial force resultant at $x = x_0 \pm \varepsilon$, $\varepsilon \to 0$ should satisfy the equation:

$$F_0(x-x_0) = \frac{1}{2}\mathrm{sgn}(x-x_0) \tag{44}$$

This equation defines the amplitude U_{00} of the wave in (43).

The power flow in the one-mode theories is defined as

$$P_1(x) = \frac{1}{2}\mathrm{Re}\left[F_0(x)\cdot \mathrm{i}\Omega u^*(x)\right] \tag{45}$$

This formula may be written explicitly:

- The Bernoulli model predicts the frequency-independent power flow:

$$P_{1B} = \frac{1}{16\sqrt{\alpha^2-1}} \tag{46}$$

- The power flow predicted by the Rayleigh–Lamb model is

$$P_{1RL} = \frac{1}{16\sqrt{(\alpha^2-1)-(1/48)(2-\alpha^2)^2\Omega^2}} \tag{47}$$

  This formula merges (46) when $\Omega \to 0$.

In the cases of three- and five-mode models, the conditions (38) and (39) are projected onto the shape functions as given in (37). Solution of the forcing problem in the framework of the five-mode theory is sought in the form:

$$\begin{aligned}
U_0(x-x_0) &= \sum_{m=1}^{5} U_m\exp(\mathrm{i}k_m|x-x_0|),\\
\Psi_1(x-x_0) &= \sum_{m=1}^{5} M_{\psi 1}U_m\exp(\mathrm{i}k_m|x-x_0|),\\
\Phi_2(x-x_0) &= \sum_{m=1}^{5} M_{\phi 2}U_m\exp(\mathrm{i}k_m|x-x_0|),\\
\Psi_3(x-x_0) &= \sum_{m=1}^{5} M_{\psi 3}U_m\exp(\mathrm{i}k_m|x-x_0|),\\
\Phi_4(x-x_0) &= \sum_{m=1}^{5} M_{\phi 4}U_m\exp(\mathrm{i}k_m|x-x_0|).
\end{aligned} \tag{48}$$

Here the wavenumbers are chosen in the same way as for the modal decomposition in the Rayleigh–Lamb forcing problem. The wavenumbers and modal coefficients are found from Eqs. (30). The generalised forces are formulated via amplitudes U_m as given in (31). The amplitude of each mode is found independently from the loading conditions (37) with the bi-orthogonality relations (35) applied.

For the five-mode model, the counterpart of (41) and (45) is

$$P_5(x) = \frac{1}{2}\mathrm{Re}\{i\Omega[F_0(x)U_0^*(x)+F_1(x)\Psi_1^*(x)+F_2(x)\Phi_2^*(x)+F_3(x)\Psi_3^*(x)+F_4(x)\Phi_4^*(x)]\} \tag{49}$$

The last two terms are omitted if the three-mode model is used.

In Fig. 5, the power flow produced by the uniformly distributed normal stresses (38) or equivalent force resultant (44) is shown as a function of the excitation frequency. As seen, the Rayleigh–Love theory prediction agrees with the exact solution much better than the prediction of the Bernoulli theory. In the frequency range displayed in this figure, the five-mode model gives the same result as the exact solution (the difference is not seen in the graph), while the three-mode model (short-dashed curve) slightly overestimates the power flow. Returning to the dispersion diagrams in Fig. 1, we notice that in this range, $0 < \Omega < 2$, only one propagating wave exists, and its wavenumber is accurately predicted by any of the one-mode theories.

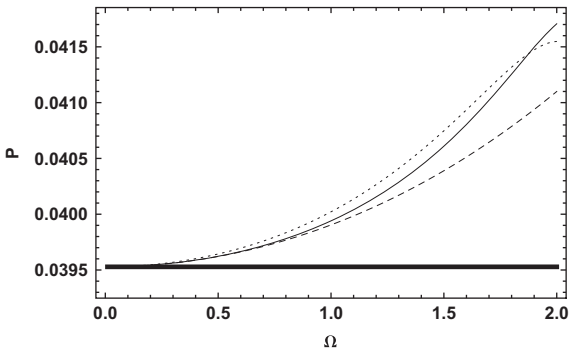

Fig. 5. The power flow in the low-frequency excitation regime: thin black curve – exact solution, short-dashed curve – the three-mode model, long-dashed curve – the Rayleigh–Love model, and thick black horizontal line – the Bernoulli model.

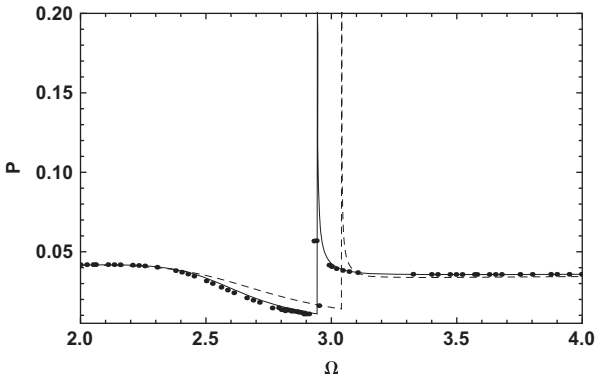

Fig. 6. The power flow in the mid-frequency excitation regime: black curve –exact solution, blue curve – the five-mode model, and green curve – the three-mode model.

In Fig. 6, the comparison is done for three- and five-modes models in the frequency range, which includes the zone where an 'anomalous' wave exists (one with group and phase velocities directed oppositely). Then the formulation of the forced responses (40) and (48) includes the wave with the positive group velocity (i.e., the counterpart of the wave which has a wavenumber shown in Fig. 1). In the vicinity of the bifurcation point, the power flow is strongly frequency-dependent, and it has a sharp peak at the frequency, where bifurcation occurs. As the excitation frequency grows, the power flow generated by the uniformly distributed normal stresses (38) becomes weakly dependent upon frequency, and, rather surprisingly, its exact magnitude is overestimated by the elementary Bernoulli theory in just 10 per cent. To explain this result, it is convenient to compare the modal contributions to the total power flow in the near field. It should be emphasised that these modal components are not identical to the modes in the exact Rayleigh–Lamb problem.

In Fig. 7, the power flow components in the five-mode theory are shown for $\Omega=2$ and $\Omega=5$. The contribution of the directly excited first component $P_1(x)=(1/2)\mathrm{Re}[F_0(x)\mathrm{i}\Omega U_0^*(x)]$ is plotted as a continuous curve; the contribution of the second component $P_2(x)=(1/2)\mathrm{Re}[F_1(x)\mathrm{i}\Omega\Psi_1^*(x)]$ is shown as dashed curve, and the third component $P_3(x)=(1/2)\mathrm{Re}[F_2(x)\mathrm{i}\Omega\Phi_2^*(x)]$ is shown as dashed–dotted curve. The last two components in formula (49) can hardly be seen in the figure, because their contributions are very small. At the frequency $\Omega=2$, only one mode is propagating (see Fig. 1). However, the condition (37) is fulfilled with all five modes involved, and series (48) for all generalised forces and displacements contains all those. Therefore, some energy leaks from the directly excited component to other ones in the near filed, see Fig. 7a. In the far field, which in this case emerges at a very short distance from the excitation point, the energy distribution establishes and does not alter. Three modes propagate at the frequency $\Omega=5$, and, therefore, the power flow distribution varies along the length as shown in Fig. 7b. The redistribution of the energy between the components of deformation is typical for multimodal waveguides.

The reported results for the loading (38) suggest that the classical Bernoulli one-mode model performs satisfactorily in this case (for which it has been derived) and this qualification holds up to rather high frequencies, as long as the power flow is concerned. The only exception is the frequency range in the vicinity of the bifurcation point, where the modal interaction strongly manifests itself.

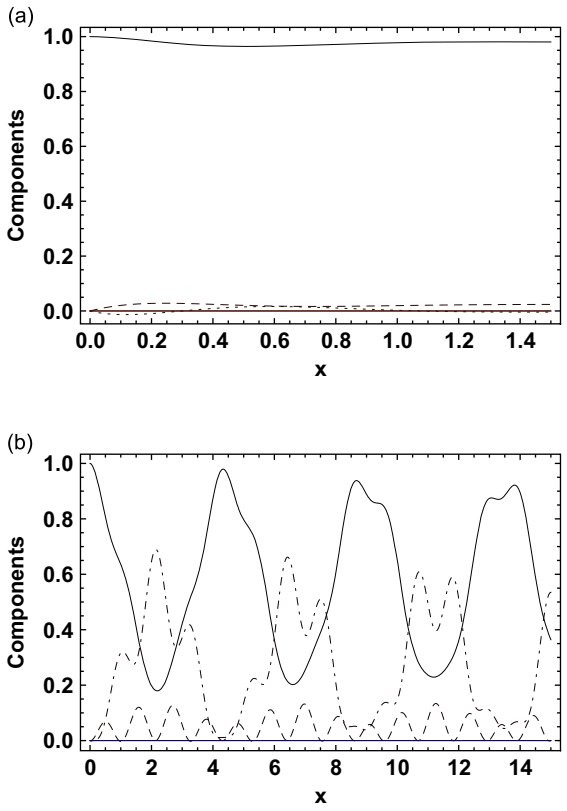

Fig. 7. The power flow distribution: (a) $\Omega = 2.$ and (b) $\Omega = 5$. Continuous curve – $P_1(x) = (1/2)\mathrm{Re}[F_0(x)\mathrm{i}\Omega U_0^*(x)]$, dashed curve – $P_2(x) = (1/2)\mathrm{Re}[F_1(x)\mathrm{i}\Omega \Psi_1^*(x)]$, and dashed–dotted curve – $P_3(x) = (1/2)\mathrm{Re}[F_2(x)\mathrm{i}\Omega \Phi_2^*(x)]$.

The situation is much different when the excitation is not produced by the uniform stress distribution (38). As an example, we consider the forcing problem with normal stresses at $x = x_0$ given as

$$\sigma_x(x_0, y) = (1 - 12y^2)\frac{1}{2}\mathrm{sgn}(x - x_0). \tag{50}$$

This distribution is self-equilibrated, and it coincides with the shape of the y-dependence of the second terms in polynomial approximations (20a) and (29a). In the exact problem formulation, this loading case is formulated as Eqs. (39) and (50). The loading conditions in the five-mode model are

$$F_0(x - x_0) = 0;\ \ \Psi_1(x - x_0) = 0;\ \ F_2(x - x_0) = \frac{1}{2}\mathrm{sgn}(x - x_0);\ \ \Psi_3(x - x_0) = 0;\ \ F_5(x - x_0) = 0. \tag{51}$$

For the three-mode model, the last two equations should be omitted in (51).

In Fig. 8, the power flow is shown in the frequency range $0 < \Omega < 1$, where only one mode propagates. However, the power flow does not vanish in the exact problem formulation as well as in three- and five-mode models. There is no contradiction, however, with the results reported in [18]. The stress distribution (50) is not identical to the shape of the evanescent wave in the transverse coordinate in this frequency range. Likewise, it is not orthogonal to the shape of the propagating wave. As the frequency grows, the power flow grows, too, because the dot product of this distribution and the transversal shape of the propagating wave become larger. The mechanism of power flow generation in the five-mode theory is illustrated in Fig. 9, which shows its distribution between components at $\Omega = 1$. The notations are the same as in Fig. 7. The power injected in the second mode is transmitted to the first one, which conveys it to the far field. The same phenomenon is known for cylindrical shells and sandwich plates with and without fluid loading. Similar to the previous excitation case, the three- and five-mode theories produce results, which agree with the exact solution very well.

As soon as the second and the third modes cut on, the power flow substantially increases as shown in Fig. 10. Similar effect has been observed in the previous case in the vicinity of bifurcation point. The distribution of the power flow between three components is illustrated in Fig. 11a just before the cut-on frequency of the second mode, in (b) just after this frequency and in (c) before the cut-on frequency of the third mode. At the frequency $\Omega = 2.5$ (Fig. 11a), only one propagating wave exists in the waveguide. Unlike the excitation case (37), it is not excited directly, and the energy injected in the waveguide as specified by condition (51) is transported to this mode in the near field. The length of this boundary layer zone is rather small, so that the constant energy distribution among the components $P_{51}(x) = (1/2)\mathrm{Re}[F_0(x)\mathrm{i}\Omega U_0^*(x)]$,

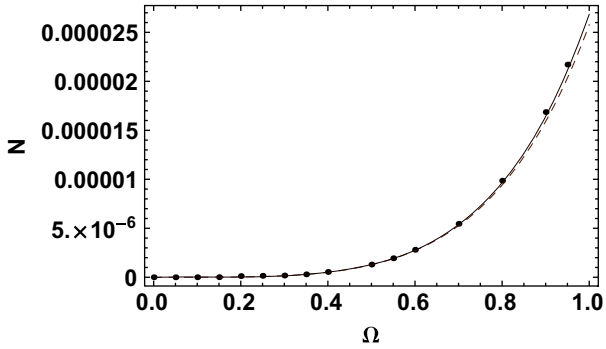

Fig. 8. The power flow produced by self-equilibrated stresses in the low-frequency excitation regime: black points – the exact solution, continuous curve – the five-mode model, and dashed curve – the three-mode model.

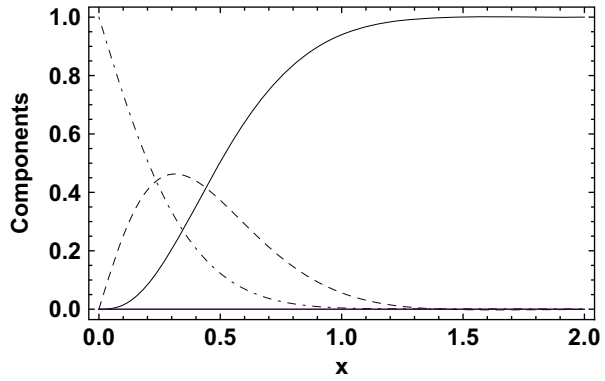

Fig. 9. The power flow distribution at $\Omega = 1$. Continuous curve – $P_1(x) = (1/2)\mathrm{Re}[F_0(x)\mathrm{i}\Omega U_0^*(x)]$, dashed–dotted curve – $P_2(x) = (1/2)\mathrm{Re}[F_1(x)\mathrm{i}\Omega \Psi_1^*(x)]$, and dashed curve – $P_3(x) = (1/2)\mathrm{Re}[F_2(x)\mathrm{i}\Omega \Phi_2^*(x)]$.

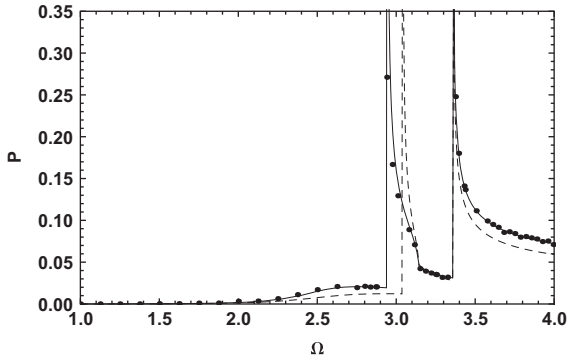

Fig. 10. The power flow produced by self-equilibrated stresses in the mid-frequency excitation regime: black points – the exact solution, continuous curve – the five-mode model, and dashed curve – the three-mode model.

$P_{52}(x) = (1/2)\mathrm{Re}[F_1(x)\mathrm{i}\Omega \Psi_1^*(x)]$ and $P_{53}(x) = (1/2)\mathrm{Re}[F_2(x)\mathrm{i}\Omega \Phi_2^*(x)]$ is established at $x \approx 2$. At higher excitation frequencies, $\Omega = 3.2$ (Fig. 11b) and $\Omega = 4$. (Fig. 11c), more than one mode propagates in the waveguide. Therefore, the balance between the power flow components varies along its length. Similar behaviour has been reported for other multimodal waveguides (for example, helical springs in [19]). Detailed analysis of the power flow distribution in various excitation regimes lies beyond the scope of this paper.

The reported results for the excitation case (50) and (51) agree with the remarks on the applicability of Saint-Venant's principle in elasto-dynamics [20,21]. Indeed, the force and moment resultants of the stress distribution (50) equal zero. Nonetheless, these self-equilibrated stresses produce a non-vanishing power flow, which is strongly frequency-dependent. Obviously, in the excitation cases like this one, the elementary one-mode models and Saint-Venant's principle are not applicable.

Green's matrices for three- and five-mode models are directly available from solutions of the forcing problems considered here. These matrices may be used to formulate boundary integral equations for homogeneous or piece-wise

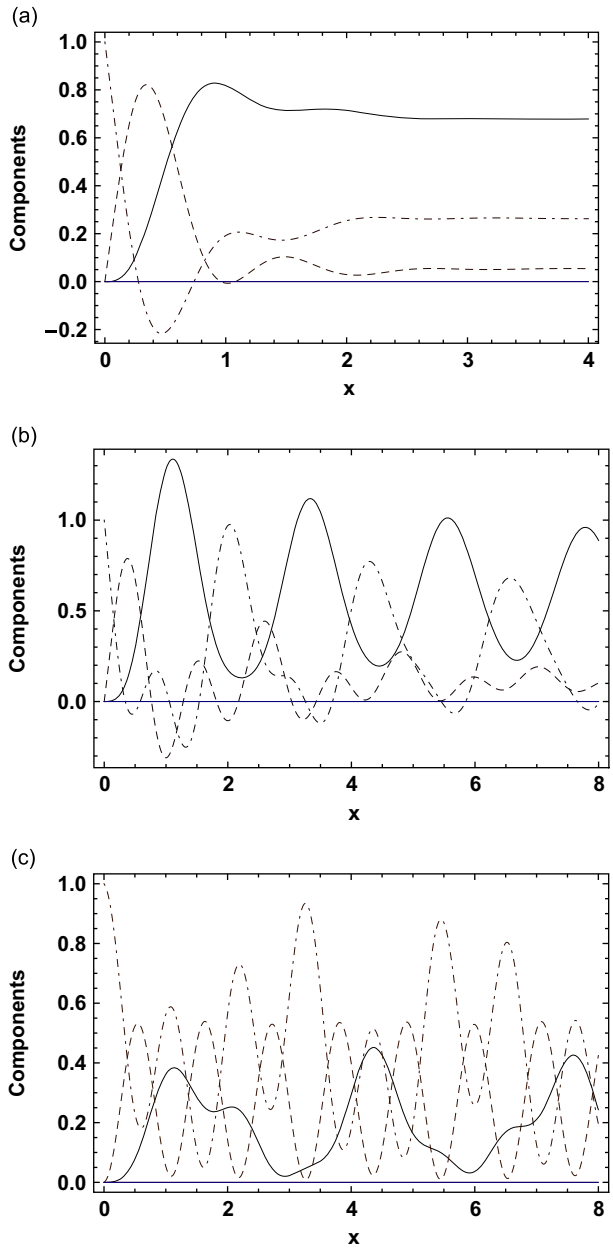

Fig. 11. The power flow distribution: (a) $\Omega = 2.5$, (b) $\Omega = 3.2$, and (c) $\Omega = 4$. Continuous curve – $P_1(x) = (1/2)\mathrm{Re}[F_0(x)\mathrm{i}\Omega U_0^*(x)]$, dashed–dotted curve – $P_2(x) = (1/2)\mathrm{Re}[F_1(x)\mathrm{i}\Omega \Psi_1^*(x)]$, and dashed curve – $P_3(x) = (1/2)\mathrm{Re}[F_2(x) \cdot \mathrm{i}\Omega \Phi_2^*(x)]$.

homogeneous layers of a finite length. Computation of eigenfrequencies and analysis of forced vibration of such layers can easily be done by means of this method (see analogous analysis for a helical spring in [19]), but this task lies beyond the scope of the present paper.

7. Conclusions

We have shown that the hierarchy of inertia-corrected multimode approximations can be reliably used to analyse waveguide properties of a straight elastic layer of constant thickness with traction-free surfaces. Accuracy of these approximations is controlled by the amount of terms retained in expansions of displacements on Legendre polynomials. It is found out and explained that, if the axial displacement is expanded with m terms, then the expansion for the transverse displacement should contain $m-1$ terms. Derivation of governing equations at each approximation level by means of Hamilton's principle yields the forcing and boundary conditions for the layer of a finite length. The classical one-mode

theories are derived by these means and shown to give asymptotically accurate predictions of wavenumbers in the low-frequency limit. For higher-order approximations, the inertia correction method is proposed, which provides an excellent agreement between locations of exact and approximate dispersion curves.

The forcing problem has been solved for generic excitation cases with the bi-orthogonality conditions used. As demonstrated, an accurate prediction of location of dispersion curves entails high accuracy in the power flow computations. The solutions of forcing problems are discussed in view of Saint-Venant's principle. As shown, the excitation by self-balanced distributions of normal stresses produces non-vanishing power flow even in the low frequency range. This result indicates that, similar to elasto-dynamics, Saint-Venant's principle is not applicable for high-order multimode models.

References

[1] R.D. Mindlin, in: J. Yang (Ed.), *An Introduction to the Mathematical Theory of Vibrations of Elastic Plates*, World Scientific, Singapore, 2006.
[2] J.D. Achenbach, *Wave Propagation in Elastic Solids*, North-Holland, Amsterdam, 1973.
[3] J. Miklowitz, *The Theory of Elastic Waves and Waveguides*, North-Holland, Amsterdam, 1978.
[4] J.D. Kaplunov, E.Yu. Kossovich, E.V. Nolde, *Dynamics of Thin Walled Elastic Bodies*, Academic Press, San Diego, London, 1991.
[5] I.T. Selezov, Hyperbolic models of wave propagation in rods, plates and shells, *Mekhanika Tverdogo Tela* 29 (1994) 64–77 (in Russian).
[6] G. Bostrom, P. Johansson, P. Olsson, On the rational derivation of a hierarchy of dynamic equations for a homogeneous, isotropic, elastic plate, *International Journal of Solids and Structures* 38 (2001) 2487–2501.
[7] L.I. Slepyan 1973 Transient Elastic Waves Sudostroenie, Leningrad (in Russian).
[8] J.F. Doyle, *Wave Propagation in Structures*, Springer, New York, 1997.
[9] C.J. Chapman, S.V. Sorokin, The finite-product method in the theory of waves and stability, *Proceedings of the Royal Society of London A* 466 (2010) 471–491.
[10] V.I. Erofeev, V.V. Kazhaev, N.P. Semerikova, 2002 Waves in Rods. Dispersion. Dissipation. Non-linearity. Fizmatlit Moscow (in Russian).
[11] M. Krawczuk, J. Grabowska, M. Palacz, Longitudinal wave propagation. Part I – comparison of rod theories, *Journal of Sound and Vibration* 295 (2006) 461–478.
[12] R.D. Mindlin, M.A. Medick, Extensional vibrations of elastic plates, *Transactions of the ASME Journal of Applied Mechanics* 26 (1959) 561–569.
[13] S.V. Sorokin, C.J. Chapman, A hierarchy of rational Timoshenko dispersion relations, *Journal of Sound and Vibration* 330 (2011) 5460–5473.
[14] S. Wolfram, *Mathematica: A System for Doing Mathematics by Computer*, Addison-Wesley Publishing Co. Reading, MA, 1991.
[15] J. Achenbach, *Reciprocity in Elastodynamics*, Cambridge University Press, Cambridge, UK, 2003.
[16] B. Karp, Generation of symmetric Lamb waves by non-uniform excitations, *Journal of Sound and Vibration* 312 (2008) 195–209.
[17] S.V. Sorokin, On the bi-orthogonality conditions for multi-modal elastic waveguides, *Journal of Sound and Vibration* 332 (2013) 5606–5617.
[18] E. Babenkova, J.D. Kaplinov, Radiation conditions for a semi-infinite elastic strip, *Proceedings of the Royal Society of London A* 401 (2005) 1163–1179.
[19] S.V. Sorokin, The Green's matrix and the boundary integral equations for analysis of time-harmonic dynamics of elastic helical springs, *Journal of Acoustical Society of America* 129 (2011) 1315–1323.
[20] V.V. Novozhilov, L.I. Slepyan, On Saint-Venant's principle in the dynamics of beams PMM, *Journal of Applied Mathematics and Mechanics* 29 (1965) 261–281 (in Russian).
[21] B. Karp, Dynamic equivalence, self-equilibrated excitation and Saint-Venant's principle for an elastic strip, *International Journal of Solids and Structures* 46 (2009) 3068–3077.